*Reprinted from*

JOURNAL OF THE PHYSICAL SOCIETY OF JAPAN

JOURNAL OF THE PHYSICAL SOCIETY OF JAPAN

http://jpsj.jpap.jp/

FULL PAPER

# Anisotropic Velocity Fluctuations and Particle Diffusion in Sedimentation

Adnan HAMID and Ryoichi YAMAMOTO

J. Phys. Soc. Jpn. **82** (2013) 024004

Journal of the Physical Society of Japan **82** (2013) 024004 **FULL PAPERS**
http://dx.doi.org/10.7566/JPSJ.82.024004

# Anisotropic Velocity Fluctuations and Particle Diffusion in Sedimentation

Adnan HAMID* and Ryoichi YAMAMOTO†

*Department of Chemical Engineering, Kyoto University, Kyoto 615-8510, Japan*

(Received October 6, 2012; accepted December 3, 2012; published online January 17, 2013)

Direct numerical simulations were performed using a smooth profile method to investigate the steady-state sedimentation of monodisperse spherical particles in an incompressible fluid at finite Peclet numbers $0 \leq Pe \leq 115$. Hydrodynamic interactions caused strong fluctuations in the instantaneous velocity of the particles around the mean settling velocity. We found that the amplitude of these velocity fluctuations increases in direct proportion with the square of the Stokes velocity at higher Peclet numbers, where sedimentation is dominated by non-equilibrium hydrodynamic fluctuations. The diffusive behaviour of the particles was observed to be in a steady state over long time scales, and the steady-state self-diffusion coefficient was found to increase linearly with the Peclet number. Our results provide new insights into the anisotropy of vertical and horizontal diffusion. This anisotropy increases with an increasing Peclet number, plateauing at a high Peclet number.

KEYWORDS: direct numerical simulation, smooth profile method, sedimentation, diffusion anisotropy, Peclet number

## 1. Introduction

The sedimentation of monodisperse colloidal particles is relevant to modern chemical and petroleum industries. Although many experimental,[1–6] theoretical,[7–9] and numerical[10–24] investigations have been performed to provide a basic understanding of sedimentation, knowledge of the long-range interactions between particles remains incomplete. These inter-particle interactions, caused by fluid flow, are referred to as hydrodynamic interactions (HIs). The first significant progress in sedimentation research was made by Stokes,[25] who calculated the sedimentation velocity of a single sphere as, $V_s^{\phi=0} = (2/9)ga^2(\rho_p - \rho_f)/\eta$, where $a$ is the particle radius, $\rho_p$ is the particle density, $\rho_f$ is the fluid density, $g$ is the gravitational acceleration, and $\eta$ is the fluid viscosity. The effect of the volume fraction on the mean settling velocity, in the form $V_s = V_s^{\phi=0}(1 - k\phi)$, was later established by Batchelor[26] for the dilute limit $\phi \ll 1$, where $\phi$ is the particle volume fraction. This decrease in velocity is attributed to the fluid back flow. The value of $k$ was found to be 6.55 for a uniform particle distribution, which is suitable for most of the experimental configurations.[27] Each particle produces a velocity field during sedimentation under a creeping flow condition that affects the motion of the other particles. This velocity field causes a change in the microstructure or position of the particles during sedimentation, thereby resulting in long-range HIs between the particles. These long-range HIs cause fluctuations in the instantaneous particle velocity around the mean settling velocity and largely depend upon the system size, volume fraction and polydispersity.

Theoretical results[7–9] and early simulations[13] suggest that velocity fluctuations converge to a finite value depending on the size of the container, whereas experiments[1,2] show no such dependency. Furthermore, fluctuation magnitudes are strongly anisotropic with vertical velocities being greater than horizontal velocities. These velocity fluctuations are found to be strongly dependent on volume fraction and aspect ratio (i.e., the ratio of the vertical to horizontal lengths) in simulations,[4,11,12] whereas experiments[1] didn't observe such dependency. This contradiction between experiment and simulation results was solved by Segre et al.[4] by introducing the concept of a characteristic swirl size or correlation length; i.e., velocity fluctuations are explained as a function of cell size, only when the cell size is less than the swirl size. These results were later confirmed by Ladd[14] using lattice Boltzmann simulations. Although the quantitative and qualitative behaviour of these velocity fluctuations is well understood, the screening mechanism for the velocity fluctuations remains unclear (i.e., the manner in which correlations in the fluctuations decay in time and space). Shaqfeh and Koch[8] proposed a Debye-like screening, whereas Ramaswamy[28] proposed a stochastic convection-diffusion model; however, these ideas were not confirmed by the computer simulations of Ladd et al.[10–14] Hinch[9] suggested another mechanism, in which the bottom wall acts as a sink for fluctuations, that was confirmed using simulations.[13,14] Some authors[6,14] posit that stratification and polydispersity also play key roles in screening. Additional details can be found in a review paper by Guazzelli.[29]

Self-diffusion is one of the most important parameters of sedimentation due to its role in mixing and other chemical processes. Although the discovery and recognition of the anomalous behaviour of particle diffusion in sedimentation is relatively new, the subject has already captured the attention of a growing number of researchers in diverse fields, including the study of suspension mechanics, fluidization, materials processing and granular flows. This diffusion is referred to as hydrodynamic diffusion because its origin lies in the HIs between the particles.

Similar to velocity fluctuations, diffusion is also strongly anisotropic, and the vertical diffusion is greater than the horizontal diffusion. This anisotropic behaviour arises from the anisotropic nature of the velocity fluctuations and their relaxation times.[30] Early simulations[10] on self-diffusion observed a large value for the anisotropy of vertical and horizontal diffusion. This large anisotropy was later corrected by increasing the volume fraction and aspect ratio of the periodic box.[11,20] Despite the importance of hydrodynamic diffusion in chemical industrial research, only a limited number of simulations[10,11,19,20] have been performed to address its behaviour.

The non-equilibrium properties of colloidal particles are difficult to simulate because they involve long-range, many-

body HIs that require enormous temporal and spatial scales. A number of different methods[10,19,20] are available to simulate non-equilibrium colloidal phenomena; excellent reviews of these methods are presented by Padding et al.[18] and Ladd et al.[15] We performed a direct numerical simulation (DNS) using the smooth profile (SP) method, which replaces the original sharp boundaries between the particle and the host fluid with a diffuse interface of finite thickness. This approach enables us to use a fixed Cartesian grid, thereby significantly improving the speed of numerical computations. The main features of our method are explained in Sect. 2.

In contrast to the majority of previous studies,[3,5,13,20] which were performed in a non-Brownian regime ($Pe \to \infty$), we focused our work in the finite Peclet number ($Pe$) regime ranging from 0 to 115, which is a significantly higher range than that studied by Padding et al.[18,19] ($Pe \leq 12$). Sedimentation at finite $Pe$ regime describes the relative effects of thermal fluctuations (caused by collisions between colloids and solvent particles) and hydrodynamic fluctuations (caused by hydrodynamic flows of solvent). In the present study, we investigated the imprints of these relative effects on the anisotropic behaviour of velocity fluctuations and diffusion. Padding et al.[17–19] were the first to study sedimentation in the finite $Pe$ using coarse-grained stochastic rotational dynamics (SRD) simulations. In SRD, the highest achievable $Pe$ is limited by the constraints on the Mach and Reynolds numbers ($Re$), whereas in the SP method, the highest $Pe$ is limited only by $Re$. Consequently, a wide range of $Pe$ is achievable, using our method. The present work validates the work of Padding[17–19] and extends it to $Pe \leq 115$. This paper also provides new insights into the anisotropic behaviour of diffusion at finite $Pe$. Section 2 explains the simulation method, and Sect. 3 describes selection of the working parameters. The results are provided in Sect. 4, and we present conclusions based on our work in Sect. 5.

## 2. Simulation Method

In this section, we briefly explain the salient features of our method. The detailed formulas, algorithm and applicability of the SP method can be found in previous publications.[31–38] In the SP method, the colloid surface is not treated as a sharp interface lacking thickness; rather, an intermediate region is introduced at the surface. This intermediate region or interface has a width comparable to the grid spacing, and the colloid's density profile is defined such that it changes smoothly within that interface. Quantities such as the velocity and pressure are defined over the entire computational domain, which includes the colloid as well as the solvent. A smooth profile function $0 \leq \phi(\boldsymbol{x}, t) \leq 1$ is used to distinguish between the fluid and particle domains. Here, $\phi = 0$ stands for fluid domain, and $\phi = 1$ indicates the particle domain.

For an arbitrary particle $i$, the motion of the colloidal particles is obtained by solving Newton's equations of motion:

$$M_i \dot{\boldsymbol{V}}_i = \boldsymbol{F}_i^{\mathrm{H}} + \boldsymbol{F}_i^{\mathrm{c}} + \boldsymbol{F}_i^{\mathrm{ext}} + \boldsymbol{G}_i^{\mathrm{V}}, \quad \dot{\boldsymbol{R}}_i = \boldsymbol{V}_i, \tag{1}$$

$$\boldsymbol{I}_i \cdot \dot{\boldsymbol{\Omega}}_i = \boldsymbol{N}_i^{\mathrm{H}} + \boldsymbol{N}_i^{\mathrm{ext}} + \boldsymbol{G}_i^{\Omega}, \tag{2}$$

where $\boldsymbol{R}_i$ is the position of the particle, $\boldsymbol{V}_i$ and $\boldsymbol{\Omega}_i$ are the translational and rotational velocity of the particle, respectively. $M_i$ and $\boldsymbol{I}_i$ are the mass and moment of inertia, respectively. $\boldsymbol{N}_i^{\mathrm{H}}$ and $\boldsymbol{F}_i^{\mathrm{H}}$ are the hydrodynamic torque and force, respectively, exerted by the solvent on the particle. $\boldsymbol{F}_i^{\mathrm{ext}}$ and $\boldsymbol{N}_i^{\mathrm{ext}}$ are the external force and torque, respectively. $\boldsymbol{G}_i^{\mathrm{V}}$ and $\boldsymbol{G}_i^{\Omega}$ are the random force and torque due to thermal fluctuations, which can be described as, $\langle \boldsymbol{G}_i^n(t) \boldsymbol{G}_j^n(0) \rangle = \alpha^n \boldsymbol{I} \delta(t) \delta_{ij}$, where $\langle \boldsymbol{G}_i^n(t) \rangle = 0$ and $\alpha^n$ $(n \in \mathrm{V}, \Omega)$ is the parameter that controls the temperature of the system $T$. The actual value of the particle temperature is determined by using the long-time diffusion coefficient of the equilibrium system. When simulating a Brownian particle with HIs, the diffusion coefficient is affected by finite size effects (i.e., the artefacts arises when system size is smaller than the correlation length). These effects can be accounted for via $D_0^{\phi=0} = D_0 K(\phi)$, where $D_0^{\phi=0}$ is the thermal diffusion coefficient of a Brownian particle at infinite dilution, $D_0$ is the thermal diffusion coefficient of Brownian particles obtained for $\phi \neq 0$ and $K(\phi)$ is the coefficient that represents the effects of the finite volume fraction of dispersed particles under periodic boundary conditions.[39] Finally, the temperature of the system can be determined using the Stokes–Einstein equation, $k_{\mathrm{B}} T = 6\pi\eta a D_0^{\phi=0}$, where $k_{\mathrm{B}}$ denotes the Boltzmann constant. The detailed implementation of Brownian motion with some test cases is presented by Iwashita et al.[33–35]

The direct inter-particle interaction $\boldsymbol{F}_i^{\mathrm{c}}$ is presented as a truncated Lennard-Jones (LJ) potential with the large powers of 24 : 12, which can be defined as:

$$U_{\mathrm{LJ}}(r_{ij}) = \begin{cases} 4\epsilon \left[ \left( \dfrac{\sigma}{r_{ij}} \right)^{24} - \left( \dfrac{\sigma}{r_{ij}} \right)^{12} \right] + \epsilon & (r_{ij} \leq 2^{1/12}\sigma), \\ 0 & (r_{ij} > 2^{1/12}\sigma), \end{cases} \tag{3}$$

where $r_{ij} = |\boldsymbol{R}_i - \boldsymbol{R}_j|$. The parameters $\sigma$ and $\epsilon$ denote the length and energy units of the LJ potential, respectively, where $\sigma = 2a$ represents the particle diameter.

In the SP method, the solvent motion is obtained by solving the modified Navier–Stokes equation for the total velocity field $\boldsymbol{v}$ and pressure field $p$ under the condition of incompressibility ($\nabla \cdot \boldsymbol{v} = 0$) as follows:

$$\rho_{\mathrm{f}} (\partial_t \boldsymbol{v} + \boldsymbol{v} \cdot \nabla \boldsymbol{v}) = -\nabla p + \eta \nabla^2 \boldsymbol{v} + \rho_{\mathrm{f}} \phi \boldsymbol{f}_{\mathrm{p}}. \tag{4}$$

The rigidity of the particle and fluid/particle non-slip boundary conditions are incorporated via the body force $\phi \boldsymbol{f}_{\mathrm{p}}$.[31,32]

A similar smooth profile[40] was adopted in the previously proposed fluid particle dynamics (FPD) method, where particles are modelled as a highly viscous fluid. In contrast, we treated particles as non-deformable solids such that no additional constraint arises. Moreover, Luo et al.[41] has performed error estimation and comparison of SP method with force coupling method (FCM)[42] and a well-resolved DNS[43] for several problems. They found that the SP method is resolving the near-field flows as well as the far-field flows accurately. Furthermore, they established after the rigorous analysis that compared to FCM and DNS, SP method is computationally faster and advantageous for simulating moving particles because it avoids the complex discretizations around the particles.

The Peclet number, which is the ratio of convection to diffusion, can be defined as

$$Pe = \frac{aV_s^{\phi=0}}{D_0}. \tag{5}$$

One can expect HIs to play a dominant role at higher $Pe$, thereby leading to changes in the microstructure.

## 3. Simulation Parameters

A number of simulations were performed under periodic boundary conditions with $Pe$ ranging from 0 to 115 at volume fraction $\phi = 0.02$. A cubic periodic box of dimension $L = 128\Delta$ and spherical particles of size $4\Delta$ were used in all of the simulations. This particular particle size has already been used by Nakayama et al.[38] for different test cases and it accurately produced the near and far-field flows, pressure distribution, drag force and lubrication interactions. We defined $\Delta$ as the lattice spacing, which is also taken as the unit of length. For given values of $\eta$ and $\rho_f$, the remaining units of mass, time, pressure and energy are respectively defined as $\rho_f\Delta^3$, $\rho_f\Delta^2/\eta$, $\eta^2/\rho_f\Delta^2$, and $\eta^2\Delta/\rho_f$. The thermal fluctuations $k_BT$ were kept constant at $\approx$0.3, and the $\epsilon$ of the LJ potential was set at 2.5. Gravity was introduced in the $z$-direction, and $Pe$ was increased by increasing the gravity. We constrained the center of mass of fluid to avoid indefinite accelerating of the system. The parameters in the Navier–Stokes equation were set such that particle Reynolds number, $Re = \rho_f a V_s^{\phi=0}/\eta$, remained less than 0.2 (i.e., creeping flow, Stokes regime). When increasing gravity, it is important that the $Re$ remain within this creeping flow condition. The majority of the experimental studies[1,2,4,29] have been performed at very low $Re$, usually of the order of $10^{-5}$ or less. Because a relative deviation from the Stokes regime will scale with the square of $Re$, we can probe relatively high $Re$ values without straying from the relevant experimental conditions. We kept the particle to fluid density ratio 5 to have a large range of $Pe$, keeping $Re \leq 0.2$. Particles require a certain period of time after the simulation begins to acquire their steady-state velocities for a given initial configuration. We monitored the data, and only that corresponding to the steady-state velocities was used. Simulations were performed for a sufficiently long period to yield statistically meaningful data for this analysis.

The HIs are increased with the increase of $Pe$. The additional hindrance caused by these HIs changes the microstructure of the system. A quantitative measure of the microstructure at the particle scale is provided by the radial distribution function (RDF)

$$g(r) = \frac{2L^3}{N^2}\left\langle \sum_{i<j} \delta(\boldsymbol{r} - \boldsymbol{r}_{ij}) \right\rangle, \tag{6}$$

where $N$ is the total number of particles, $r = |\boldsymbol{r}|$, $\boldsymbol{r}_{ij} = \boldsymbol{R}_i - \boldsymbol{R}_j$, $\langle \cdots \rangle$ denotes an ensemble average, and the summation $\sum_{i<j}$ is taken over all particle pairs. This definition of $g(r)$ implies that $4\pi\rho g(r) r^2 \Delta r$ represents the mean number of particles in a shell of radius $r$ and thickness $\Delta r$ surrounding a particle, set at the origin.[44] Figure 1 shows the $g(r)$ for different $Pe$. The peak of the function increases with increasing $Pe$, demonstrating the formation of aggregates or clusters. This clustering was expected as random motion progressively disappears with increasing $Pe$ which in turn induces the cluster formation. The similar phenomena has also been observed by Brady et al.,[16] while investigating the relative effect of thermal and shear force. They reduced the effect of thermal fluctuations by increasing the shear rate and observed the similar cluster formation. Figure 1 also shows that the results are not distinguishable from the equilibrium results ($Pe = 0$) for $Pe = 6$, showing the strong effect of thermal fluctuations, whereas for $Pe > 6$, these results are differentiable, evincing a progressively dominating effect of HIs. A large change in the RDF between $Pe \leq 29$ and $Pe \geq 57$ indicates that HIs overpower the phenomena.

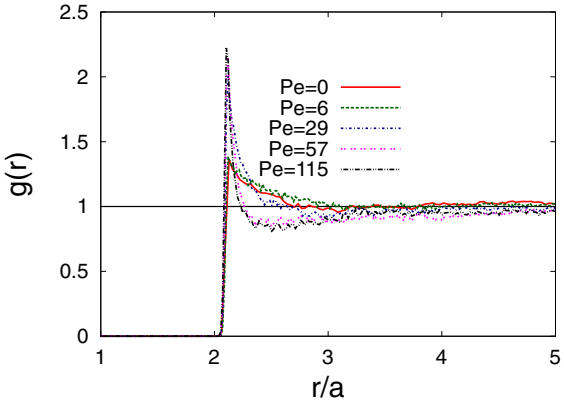


**Fig. 1.** (Color online) Radial distribution function $g(r)$ for different $Pe$. Simulations are performed in a cubic periodic box of length $L = 128$ with a particle size of $a = 4$, keeping $\phi$ and $k_BT$ constant respectively at $\approx$0.02 and 0.3.

## 4. Results and Discussion

### 4.1 Spatial correlations of velocity fluctuations

To study the effect of $Pe$ on the flow pattern, we define the following spatial correlation functions for the velocity fluctuations:

$$C_z(\boldsymbol{r}) = \frac{2L^3}{N^2}\left\langle \sum_{i<j} \delta V_{iz}\delta V_{jz}\delta(\boldsymbol{r} - \boldsymbol{r}_{ij}) \right\rangle, \tag{7}$$

where $\delta V_{iz} = V_{iz} - V_{sed}$, $V_{iz}$ is the temporal velocity of the $i$th particle in the $z$-direction, and $V_{sed} = \langle V_{iz} \rangle$ is the mean settling velocity of the particles. We define $C_z(z)$ and $C_z(x)$, with respect to the distance vector $\boldsymbol{r}$, in either the vertical $\boldsymbol{r} = z\boldsymbol{\delta}_z$ or horizontal $\boldsymbol{r} = x\boldsymbol{\delta}_x$ direction.

Figure 2 shows the decay of the spatial correlation functions of the $z$-component of velocity as a function of the vertical ($z$) and horizontal ($x$) distances, where the distance is normalized by the particle radius $a$. In the main plots of Figs. 2(a) and 2(b), the correlation functions are normalized by the initial value of the fluctuations, whereas the correlation functions in the figure insets are normalized by the square of the Stokes velocity. Figure 2(b) shows a persistent positive correlation in the direction of gravity, whereas Fig. 2(a) shows a rapid decay of all correlations in the direction perpendicular to gravity followed by a distinct region of anti-correlation similar to that observed in experiments[4] and simulations.[19] Notably, for a sufficiently large system, the horizontal correlations should decay exponentially and become negative before settling to zero. The minima of these anti-correlations is known as the correlation length[4] $\xi \approx 20a\phi^{-1/3}$, i.e., $\xi$ is twenty-fold

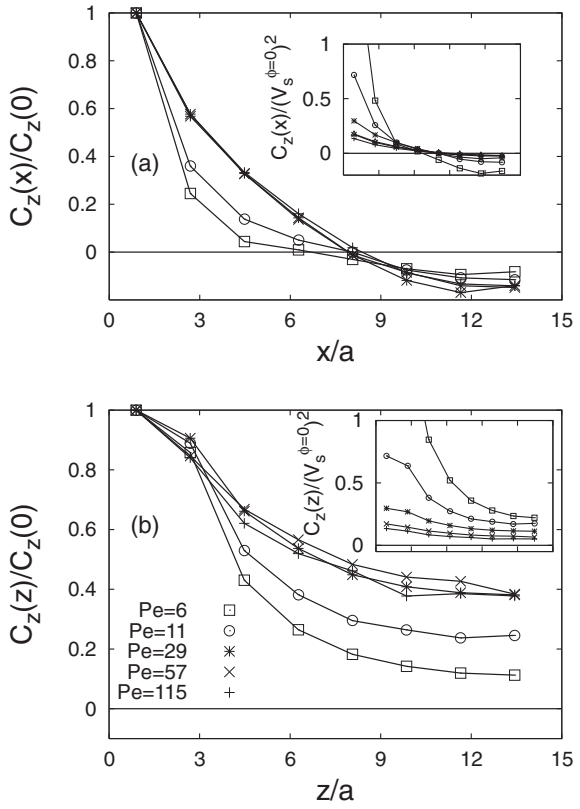


**Fig. 2.** Spatial correlation function of velocity fluctuations of the $z$-component of the velocity as a function of the distance: (a) shows the spatial correlation function perpendicular to gravity and (b) shows the spatial correlation function parallel to gravity. In the main plots, the correlation functions are normalized by the initial position fluctuations, whereas the correlation functions in the insets are normalized by the square of the Stokes velocity. The distance is normalized by the particle radius $a$.

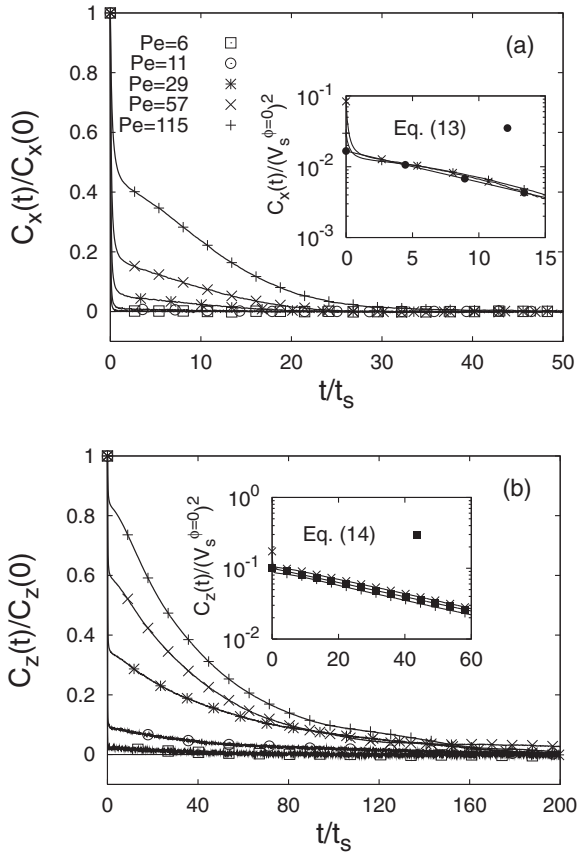


**Fig. 3.** Temporal autocorrelation functions of the velocity fluctuations of the vertical $[C_z(t)]$ and horizontal $[C_x(t)]$ components of the velocity. The main plots show the correlation functions normalized by the initial fluctuations, whereas the temporal correlation functions shown in the insets are normalized by the square of the Stokes velocity on a semi-log scale. Insets also show that at large $Pe$, these correlation functions relax exponentially of the form $C_\beta(t) = (\Delta V_{\rm H}^\beta)^2 \exp(-t/\tau_{\rm H}^\beta)$, where $\Delta V_{\rm H}^\beta$ ($\beta \in x, z$) and $\tau_{\rm H}^\beta$ denote the amplitude and the relaxation time of the hydrodynamic velocity fluctuations, respectively. Time is normalized by the Stokes time $t_{\rm s}$, where $t_{\rm s} = a/V_{\rm s}^{\phi=0}$.

greater than the inter-particle distance. Although anti-correlations are also clearly visible in our results, a larger system size is needed to verify the correlation length obtained experimentally. This determination is, however, beyond the scope of the present study.

The particle motion is affected by the finite system size in our simulations. A large system size is needed to reproduce the saturation of the velocity fluctuations, but it requires enormous computational time and resource. Therefore, most of the computational studies[10,11,14,19,20] are in the same situation as ours. The systematic experimental[2,4] and simulation[11,13] studies, however, addressed that the effects of finite system size on velocity fluctuations can be effectively explained using a concept of finite size scaling.[19] We believe that performing critical tests for the scaling concept possesses an important value.

### 4.2 *Temporal correlations of velocity fluctuations*

To differentiate between the effects of the hydrodynamic and thermal fluctuations, we define the temporal autocorrelation functions of the velocity fluctuations as follows:

$$C_x(t) = \langle V_{ix}(t) V_{ix}(0) \rangle, \tag{8}$$

$$C_z(t) = \langle \delta V_{iz}(t) \delta V_{iz}(0) \rangle. \tag{9}$$

Figure 3 shows the time decay of the correlation functions for the $z$ and $x$ components of the velocity fluctuations. Two different normalizations were used: the main plots of Fig. 3 show the temporal correlation functions normalized by the initial values $C_z(0)$ and $C_x(0)$, whereas the figure insets show the temporal correlation functions normalized by the square of the Stokes velocity in a semi-log plot. Time was normalized by the Stokes time $t_{\rm s}$, where $t_{\rm s} = a/V_{\rm s}^{\phi=0}$.

The main plots of Figs. 3(a) and 3(b) show that the relaxation time is different for the vertical and horizontal correlations, whereas the experiments of Nicolai[1] did not show a large difference at these time scales. The theory proposed by Koch[30] suggests that this difference in time scales come from the vertical periodic boundary conditions. Therefore, the time required by a particle to sample all the vertical position is much smaller than that required to sample horizontal positions. This difference in time scales can be reduced by increasing the system size. The computer simulations of Ladd[10] and padding[19] also observed the same phenomena while using vertical periodic boundary conditions. In contrast to simulations, experiments[1,4] use much larger system which reduce the difference in vertical and horizontal relaxation time. At low $Pe$, the strong effects of thermal fluctuations cause a rapid decay of correlation functions, whereas at higher $Pe$, exponential decay is evident, as shown in Fig. 3.

In an experimental study, Nicolai et al.[1)] observed an exponential relaxation of the form

$$C_\beta(t) = (\Delta V_{\mathrm{H}}^\beta)^2 \exp\left(-\frac{t}{\tau_{\mathrm{H}}^\beta}\right), \tag{10}$$

where $\Delta V_{\mathrm{H}}^\beta$ ($\beta \in x, z$) and $\tau_{\mathrm{H}}^\beta$ denote the amplitude and the relaxation time of the hydrodynamic velocity fluctuations, respectively. Hinch[9)] predicted the scaling relations

$$\Delta V_{\mathrm{H}}^\beta / V_{\mathrm{s}}^{\phi=0} = \sqrt{A_1^\beta L\phi/a}, \tag{11}$$

$$\tau_{\mathrm{H}}^\beta / t_{\mathrm{s}} = A_2^\beta \sqrt{L/(\phi a)}, \tag{12}$$

where $A_1^\beta$ and $A_2^\beta$ are constants that depend on the specific configuration of the system (e.g., the container shape, swirl size, particle shape, and polydispersity). Cunha et al.[20)] explained the scaling relations predicted by Hinch[9)] by hypothetically dividing the simulation box into two equal parts. The imbalance in the particle weight caused by variations in the particle number in both parts is balanced by the Stokes drag. Velocity fluctuations consist of thermal and hydrodynamic component. At high $Pe$, hydrodynamic fluctuations dominate the phenomena, whereas thermal fluctuations play a key role at low $Pe$. This dominant role of hydrodynamic fluctuations at higher $Pe$ causes the correlation functions to fall on the same curve when scaled with the square of the Stokes velocity, as shown in the insets of Fig. 3, which is in good agreement with the simulations.[19,20)] This normalization highlights the effect of the non-equilibrium hydrodynamic fluctuations.

The present DNS results support the following forms for the velocity autocorrelations:

$$C_x(t) = C_0(t) + (\Delta V_{\mathrm{H}}^x)^2 \exp\left(-\frac{t}{\tau_{\mathrm{H}}^x}\right), \tag{13}$$

$$C_z(t) = C_0(t) + (\Delta V_{\mathrm{H}}^z)^2 \exp\left(-\frac{t}{\tau_{\mathrm{H}}^z}\right), \tag{14}$$

where $C_0(t)$ represents the velocity autocorrelation function in the presence of thermal fluctuations but without gravity, which quantitatively becomes negligible at higher $Pe$. We continue our analysis by assuming the scaling arguments[20)] as explained in Eqs. (11) and (12). The perfectors $A_1^\beta$ and $A_2^\beta$ are determined based on exponential fits both on vertical and horizontal correlation functions as $A_1^z \approx 0.156$, $A_2^z \approx 1.08$, $A_1^x \approx 0.028$, and $A_2^x \approx 0.22$. The difference in vertical and horizontal prefactors indicates the anisotropic behaviour of velocity fluctuation with the vertical fluctuations larger than the horizontal. This anisotropy of velocity fluctuations varies from 2.5 to 4 in simulations,[10,12,20,22)] whereas experiments[1,4)] have found relatively low value of $\approx$2.5. Notably, the ratio of the vertical to horizontal hydrodynamic velocity fluctuations in this study, $\Delta V_{\mathrm{H}}^z / \Delta V_{\mathrm{H}}^x \approx 2.36$, is in good agreement with the experimental[1,4)] and simulations[22)] studies. From the asymmetry of the system induced by the gravity, velocity fluctuations are expected to be anisotropic.

### 4.3 *Anisotropic behavior of diffusion*

Diffusion refers to the fluctuating motion of particles. Individual particles lose the memory of their velocity after prolonged HIs, and thereafter follow a random-walk diffusion process. This effect is evident in the behaviour of the temporal autocorrelation functions of the velocity fluctuations and the linear growth of the mean-square displacement (MSD).

The equilibrium self-diffusion coefficient can be obtained using the Green–Kubo equation

$$D_0 = \int_0^\infty C_0(\tau)\,\mathrm{d}\tau \tag{15}$$

or the Einstein relationship

$$D_0 = \lim_{t\to\infty} \frac{1}{6t} \langle (\boldsymbol{R}_i(t) - \boldsymbol{R}_i(0))^2 \rangle. \tag{16}$$

To examine the anisotropic particle diffusion in sedimentation, we define the temporal diffusion constant both in the horizontal

$$D_x(t) = \frac{1}{2t} \langle (R_{ix}(t) - R_{ix}(0))^2 \rangle \tag{17}$$

and vertical directions

$$D_z(t) = \frac{1}{2t} \langle (R_{iz}(t) - R_{iz}(0) - V_{\mathrm{sed}}t)^2 \rangle. \tag{18}$$

Figure 4 shows the time-dependent diffusion coefficient defined by Eqs. (17) and (18) for various $Pe$. The diffusion coefficients are normalized by the equilibrium self-diffusion coefficient $D_0$, which can be found via Eq. (15) or (16) at $Pe = 0$, whereas time is normalized by the Stokes time. One can see in Fig. 4 that self-diffusion becomes highly anisotropic at higher $Pe$. We determined the long-time self-diffusion coefficients $D_\beta = \lim_{t\to\infty} D_\beta(t)$ by fitting the simulation data with

$$D_\beta(t) = D_\beta\left(1 - \exp\left[-\left(\frac{t}{\tau_r}\right)^\gamma\right]\right), \tag{19}$$

where $D_\beta$, $\tau_r$, and $\gamma$ are the fitting parameters. In Figs. 4 and 5, values of $D_z/D_0$ much larger than unity suggest that the role of HIs cannot be overlooked, even at low $Pe$. A similar phenomena was observed by Padding et al.[19)]

To understand the diffusivity, we consider the total diffusion coefficient $D$ as the sum of thermal $D_0$ and hydrodynamic diffusivity $D_{\mathrm{H}}$, where latter can be estimated via the aforementioned scaling arguments,

$$D_{\mathrm{H}}^\beta \approx (\Delta V_{\mathrm{H}}^\beta)^2 \tau_{\mathrm{H}}^\beta = A_1^\beta A_2^\beta V_{\mathrm{s}}^{\phi=0} a\phi^{1/2}(L/a)^{3/2} \tag{20}$$

$$= A_1^\beta A_2^\beta D_0 Pe\phi^{1/2}(L/a)^{3/2}. \tag{21}$$

The following simple scaling relationships are predicted for the present simulation results:

$$D_x/D_0 = 1 + A_1^x A_2^x\, Pe\, \phi^{1/2}(L/a)^{3/2} = 1 + 0.158Pe, \tag{22}$$

$$D_z/D_0 = 1 + A_1^z A_2^z\, Pe\, \phi^{1/2}(L/a)^{3/2} = 1 + 4.313Pe. \tag{23}$$

These scaling arguments indicate that the vertical and horizontal diffusion coefficients increase linearly with $Pe$, but with a smaller prefactor in the horizontal direction. Figure 5 shows a comparison of the steady-state self-diffusion coefficients with those predicted by the scaling argument. The simulation results show that diffusion coefficients increase linearly with increase of hydrodynamic fluctuations both parallel and perpendicular to gravity.

A deviation from the predicted scaling equations is evident at $Pe < 6$, which shows the transition from a thermal-fluctuations-dominated regime to a hydrodynamic-fluctuations-dominated regime. Since, above scaling rela-

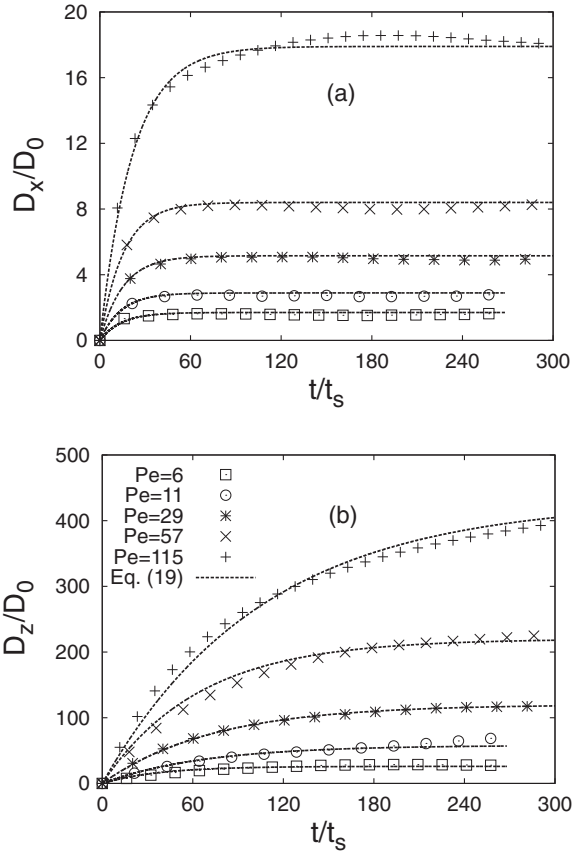


**Fig. 4.** The horizontal and vertical direction self-diffusion coefficients normalized by the equilibrium diffusion coefficient $D_0$ as a function of time at various $Pe$. Both (a) and (b) show the horizontal and vertical time-dependent self-diffusion coefficients, respectively. Time is normalized by the Stokes time. The volume fraction is set at 0.02. Dashed lines show the exponential fit on the simulation data.

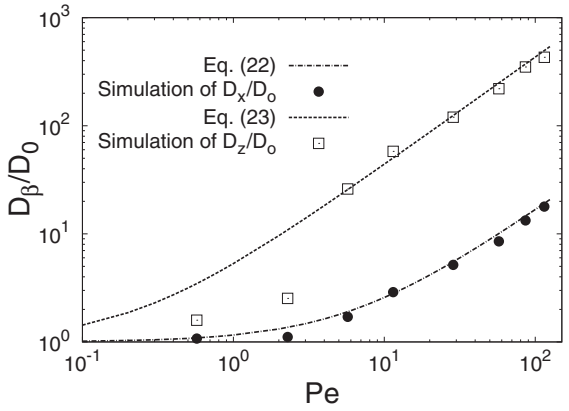


**Fig. 5.** A comparison of steady state self-diffusion coefficients $D_\beta(\beta \in x, z)$ both in vertical and horizontal direction with those predicted by scaling Eqs. (22) and (23) as a function of $Pe$. The self-diffusion coefficients are normalized by the equilibrium diffusion coefficient $D_0$.

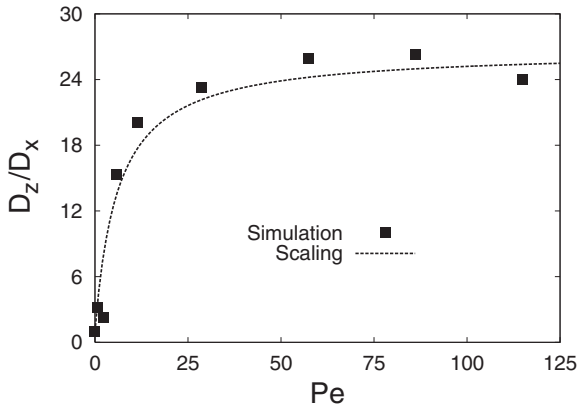


**Fig. 6.** The anisotropy of the vertical ($D_z$) and horizontal ($D_x$) self-diffusion coefficient as a function of $Pe$ at a volume fraction of 0.02. The scaling line is obtained by dividing the Eq. (23) with Eq. (22).

tions are derived by adding pure thermal and hydrodynamic forces. Therefore, scaling relations are expected to work well at either very low $Pe$ (thermal force dominates) or high $Pe$ (hydrodynamic force dominates). Hence, deviation from the scaling relations indicates the interplay between these two forces. Our simulations show good agreement with the predictive Eqs. (22) and (23), determined from scaling arguments. These scaling arguments also indicate that anisotropy in diffusion increases with the increase of $Pe$, reaching a steady value at high $Pe$. From a simple dimensional analysis of Eq. (23), one can also predict that $D_z/aV_s^{\phi=0}$ should collapse to a single value at higher $Pe$. In our simulation, this value $\approx 4$ and is in good agreement with experimental results.[1,2)]

The majority of diffusion research is focused in the non-Brownian regime, and anisotropic behaviour of diffusion at finite $Pe$ has not yet been explored. We have attempted to investigate this anisotropic behaviour at finite $Pe$ and found that it increases with increasing $Pe$ and settles to a steady value at higher $Pe$, as shown in Fig. 6. This observation suggests that the effect of thermal fluctuations is significant at $Pe \leq 29$ before HIs begin to dominate the phenomena. We can predict the anisotropic behaviour of the diffusion at finite $Pe$ with scaling arguments found in Eqs. (22) and (23). Our data shows good agreement with the predicted diffusion anisotropy, as shown in Fig. 6.

Because the diffusivity is the product of $\Delta V_H^2$ and $\tau_H$, a higher diffusion anisotropy value was expected. This higher value originates from the difference in vertical and horizontal relaxation times. The diffusion anisotropy can be reduced by increasing the aspect ratio of the simulation box.[30)] An increase in the aspect ratio reduces the difference in vertical and horizontal relaxation times and hence the diffusion anisotropy. Nicolai[1)] achieved diffusion anisotropy in a non-Brownian regime of $D_z/D_x \simeq 7$ at $\phi = 0.05$, whereas Padding et al.[19)] reported the same value in simulations using a periodic box of aspect ratio of 3 at $\phi = 0.04$. Ladd[12)] observed a much higher value of 77 in a cubic simulation box for $\phi = 0.05$. This higher value was attributed to the small system size and the full periodic boundary conditions that were used. Cunha et al.[20)] observed the anisotropy to be 10 using an aspect ratio of 3 at $\phi = 0.03$. To quantitatively compare the anisotropy values using an experimental system, one should consider that our simulations depend on the system size, whereas experiments do not. Another possible explanation for the discrepancy between simulation and experimental results is the presence of a side wall, which creates microstructure inhomogeneity over time. The presence of even a small extent of

**Table I.** Comparison of the observed diffusion anisotropy with previously published experimental and simulated data. Nicolai performed these experiments with a ratio of vessel width to particle radius ranging from 51 to 212. Ladd performed these simulations in a cubic periodic box at $Re = 0.17$ with 32 spheres. Padding and Cunha performed simulations with an aspect ratio of 3.

| | $\phi$ | $D_z/D_x$ |
|---|---|---|
| Present Study | 0.02 | 25 |
| Nicolai[2)] | 0.05 | 5–7.4 |
| Ladd[12)] | 0.05 | 77 |
| Padding[19)] | 0.04 | 7 |
| Cunha[20)] | 0.03 | 10 |

polydispersity can also temper the diffusion. Experimental and simulated diffusion anisotropy results are summarized in Table I.

## 5. Concluding Remarks

In conclusion, we studied the steady-state sedimentation at finite *Pe* by DNS using the SP method in a spatially unscreened regime. The present study focused on the relative effects of thermal and hydrodynamic fluctuations on anisotropic behaviour of velocity fluctuation and self-diffusion. We observed that the thermal fluctuations are noticeable at $Pe \leq 29$, before HIs significantly dominate the phenomena. We found that the amplitude of the velocity correlation scales with the square of the Stokes velocity at large *Pe*, with vertical hydrodynamic velocity fluctuations 2.36 times larger than the horizontal hydrodynamic velocity fluctuations. In addition, we successfully tested the scaling for hydrodynamic velocity fluctuations, predicted by Hinch[9)] on our system and used it to evaluate the anisotropic behaviour of diffusion. We inferred that the long time steady-state self-diffusion coefficient increased with the increase of *Pe* both in the direction of gravity and perpendicular to gravity and it became highly anisotropic at high *Pe*, with a vertical self-diffusion coefficient higher than the horizontal, in good agreement with the scaling. This anisotropy of the vertical and horizontal diffusion increased as a function of *Pe* and levelled off at higher *Pe*. Our results endorsed the findings of Koch,[30)] who suggested that the change in the velocity fluctuations with the box shape is relatively modest, however diffusion coefficients changes rather significantly with the aspect ratio. Similar to Koch findings, velocity fluctuations in our simulations are also in good agreement with the other simulation[19,20)] and experimental results,[1)] whereas diffusion anisotropy is higher due to large vertical relaxation time. So far, researchers have paid little attention to the anisotropic behaviour of diffusion at finite *Pe*. We will extend our simulation studies to investigate the salient features of this diffusion anisotropy at large volume fractions, various system sizes, and large *Re*. Extensive simulations are under way to study such situations specially to verify the scaling arguments at different volume fractions and system sizes.

## Acknowledgements

This work was supported by JSPS KAKENHI 23244087. The author would like to extend his gratitude to Dr. Takahiro Murashima, Dr. Hideyuki Mizuno, and Dr. John Molina for their useful discussions and suggestions.

*hamid@cheme.kyoto-u.ac.jp
†ryoichi@chem.kyoto-u.ac.jp

1) H. Nicolai, B. Herzhaft, E. J. Hinch, L. Oger, and E. Guazzelli: Phys. Fluids **7** (1995) 12.
2) H. Nicolai and E. Guazzelli: Phys. Fluids **7** (1995) 3.
3) H. Nicolai, Y. Peysson, and E. Guazzelli: Phys. Fluids **8** (1996) 855.
4) P. N. Segrè, E. Helbolzheimer, and P. M. Chaikin: Phys. Rev. Lett. **79** (1997) 2574.
5) P. N. Segrè, F. Liu, P. Umbanhowar, and D. A. Weitz: Nature **409** (2001) 594.
6) P. N. Segrè: Phys. Rev. Lett. **89** (2002) 254503.
7) R. E. Caflisch and J. H. C. Luke: Phys. Fluids **28** (1985) 759.
8) D. L. Koch and E. S. G. Shaqfeh: J. Fluid Mech. **224** (1991) 275.
9) E. J. Hinch: in *Disorder and Mixing*, ed. E. Guyon, Y. Pomeau, and J. P. Nadal (Kluwer Academic, Dordrecht, 1988).
10) A. J. C. Ladd: Phys. Fluids A **5** (1993) 299.
11) A. J. C. Ladd: Phys. Rev. Lett. **76** (1996) 1392.
12) A. J. C. Ladd: Phys. Fluids **9** (1997) 491.
13) A. J. C. Ladd: Phys. Rev. Lett. **88** (2002) 048301.
14) N. Q. Nguyen and A. J. C. Ladd: J. Fluid Mech. **525** (2005) 73.
15) A. J. C. Ladd and R. Verberg: J. Stat. Phys. **104** (2001) 1191.
16) G. Bossis and J. F. Brady: J. Chem. Phys. **87** (1987) 5437.
17) J. T. Padding and A. A. Louis: Phys. Rev. Lett. **93** (2004) 220601.
18) J. T. Padding and A. A. Louis: Phys. Rev. E **74** (2006) 031402.
19) J. T. Padding and A. A. Louis: Phys. Rev. E **77** (2008) 011402.
20) F. R. Cunha, G. C. Abade, A. J. Sousa, and E. J. Hinch: J. Fluids Eng. **124** (2002) 957.
21) S. Y. Tee, P. J. Mucha, M. P. Brenner, and D. A. Weitz: Phys. Fluids **19** (2007) 113304.
22) M. C. Miguel and R. Pastor-Satorras: Europhys. Lett. **54** (2001) 45.
23) X. Yin and D. L. Koch: Phys. Fluids **20** (2008) 043305.
24) E. Kuusela, J. M. Lahtinen, and T. Ala-Nissila: Phys. Rev. E **69** (2004) 066310.
25) G. G. Stokes: *Mathematical and Physical Papers* (Johnson Reprint Corporation, New York, 1966).
26) G. K. Batchelor: J. Fluid Mech. **52** (1972) 245.
27) J. M. Ham and G. M. Homsy: Int. J. Multiphase Flow **14** (1988) 533.
28) A. Levine, S. Ramaswamy, E. Frey, and R. Bruinsma: Phys. Rev. Lett. **81** (1998) 5944.
29) E. Guazzelli and J. Hinch: Annu. Rev. Fluid Mech. **43** (2011) 97.
30) D. L. Koch: Phys. Fluids **6** (1994) 2894.
31) Y. Nakayama and R. Yamamoto: Phys. Rev. E **71** (2005) 036707.
32) Y. Nakayama, K. Kim, and R. Yamamoto: Eur. Phys. J. E **26** (2008) 361.
33) T. Iwashita, Y. Nakayama, and R. Yamamoto: J. Phys. Soc. Jpn. **77** (2008) 074007.
34) T. Iwashita and R. Yamamoto: Phys. Rev. E **79** (2009) 031401.
35) T. Iwashita, Y. Nakayama, and R. Yamamoto: Prog. Theor. Phys. Suppl. **178** (2009) 86.
36) Y. Nakayama, K. Kim, and R. Yamamoto: Adv. Powder Technol. **21** (2010) 206.
37) KAPSEL website [http://www-tph.cheme.kyoto-u.ac.jp/kapsel/].
38) Y. Nakayama, K. Kim, and R. Yamamoto: Eur. Phys. J. E **26** (2008) 361.
39) A. A. Zick and G. M. Homsy: J. Fluid Mech. **115** (1982) 13.
40) H. Tanaka and T. Araki: Phys. Rev. Lett. **85** (2000) 1338.
41) X. Luo, M. R. Maxey, and G. E. Karniadakis: J. Comput. Phys. **228** (2009) 1750.
42) M. R. Maxey and B. K. Patel: Int. J. Multiphase Flow **27** (2001) 1603.
43) R. M. Kirby, T. C. Warburton, S. J. Sherwin, A. Beskok, and G. E. Karniadakis: Proc. 2nd Int. Conf. Computational Technologies for Fluid/Thermal/Chemical Systems with Industrial Applications, 1999.
44) D. C. Rapaport: *The Art of Molecular Dynamics Simulation* (Cambridge University Press, Cambridge, U.K., 2004) 2nd ed., p. 90.